Optimal control of Raman pulse sequences for atom interferometry

Optimal control of Raman pulse sequences for atom interferometry

Jack Saywell,[1,*] Max Carey,[1,†] Mohammad Belal,[1] Ilya Kuprov,[2] and Tim Freegarde[1]

[1] *School of Physics & Astronomy, University of Southampton, Highfield, Southampton, SO17 1BJ, UK*
[2] *School of Chemistry, University of Southampton, Highfield, Southampton, SO17 1BJ, UK*

(Dated: January 14, 2020)

We present the theoretical design and experimental implementation of mirror and beamsplitter pulses that improve the fidelity of atom interferometry and increase its tolerance of systematic inhomogeneities. These pulses are designed using the GRAPE optimal control algorithm and demonstrated experimentally with a cold thermal sample of ^{85}Rb atoms. We first show a stimulated Raman inversion pulse design that achieves a ground hyperfine state transfer efficiency of 99.8(3)%, compared with a conventional π pulse efficiency of 75(3)%. This inversion pulse is robust to variations in laser intensity and detuning, maintaining a transfer efficiency of 90% at detunings for which the π pulse fidelity is below 20%, and is thus suitable for large momentum transfer interferometers using thermal atoms or operating in non-ideal environments. We then extend our optimization to all components of a Mach-Zehnder atom interferometer sequence and show that with a highly inhomogeneous atomic sample the fringe visibility is increased threefold over that using conventional π and $\pi/2$ pulses.

* j.c.saywell@soton.ac.uk
† max.carey@soton.ac.uk

I. INTRODUCTION

Atom interferometers [1] are the matterwave analogues of optical interferometers. Slow, massive atomic wavepackets replace the photons that are divided to follow separate spatial paths before being recombined to produce interference; and, in place of the mirrors and beamsplitters, carefully-timed resonant laser pulses split, steer and recombine the wavepackets. Atom interferometers have already demonstrated unprecedented performance for inertial measurement, with potential applications such as navigation [2–5], the detection of gravitational waves [6, 7], measurements of the fine structure constant [8, 9] and the Newtonian gravitational constant [10], and investigations of dark energy [11, 12].

As with an optical interferometer, the sensitivity of an atom interferometer depends upon the lengths and separation of the interfering paths and the coherence and number of quanta detected. Whereas optical interferometers are possible on the kilometre scale using ultra-stable lasers and optical fibre components, the path separations in atom interferometers result from momentum differences of only one or a few photon recoils, and expansion of the atom cloud limits the interferometer duration. Large momentum transfer (LMT) interferometers increase the path separation by employing repeated augmentation pulses to impart multiple photon impulses [13], but any inherent sensitivity improvements thus achieved are, in practice, limited by a reduction in fringe visibility resulting from the accrued effect of repeated operations with imperfect fidelity [14, 15]. LMT interferometers typically rely on an atomic sample with a narrow initial momentum distribution [15, 16], with Bloch oscillations [17–19] and Bragg diffraction [20–22] demonstrating the greatest separation, but filtering the atomic sample in this way to reduce the effects of inhomogeneities and cloud expansion involves lengthier preparation and causes a fall in the signal-to-noise ratio because fewer atoms are measured.

For applications such as inertial navigation where both the sensitivity and repetition rate are important, techniques are required that are more tolerant of experimental and environmental inhomogeneities in laser intensity, magnetic field, atom velocity and radiative coupling strength. Adiabatic transfer [23–27] allows robust, high-fidelity state transfer, but is necessarily a slow process not suited to preparing or resolving superpositions [28]. Composite and shaped pulses [29–32] are attractive alternatives. Originally developed for nuclear magnetic resonance (NMR) spectroscopy, composite pulses are concatenated sequences of pulses with tailored phases and durations that can replace the fractional Rabi oscillations in atom interferometers and increase the tolerance of inhomogeneities in the atom-laser interaction [14, 33].

These pulse shapes can be tailored and improved using optimal control techniques [34–36] that have been applied extensively in NMR [37–43], and have also been successfully demonstrated in nitrogen-vacancy (NV) magnetometry [44], ultra-cold molecule stabilization [45] and the control of Bose-Einstein condensates [46–48].

We have previously investigated the application of optimal control techniques to the optimization of mirror pulses for interferometry, showing computationally how this can maximize interferometer contrast by compensating for realistic experimental inhomogeneities in detuning and coupling strength [49]. We now build on this, presenting the theory and experimental implementation of a high-fidelity inversion pulse and a novel approach to optimizing an entire 3-pulse interferometer sequence.

Our inversion pulse achieves 99.8(3)% transfer between the two hyperfine ground states in a thermal sample of ^{85}Rb where a rectangular π pulse achieves only 75(3)%, with a greater velocity acceptance than existing composite and shaped pulses making it particularly suited for LMT applications. Our optimized 3-pulse interferometer demonstrates a threefold increase in the experimental fringe visibility with a 94(4) μK atom sample compared to a conventional Mach-Zehnder interferometer using rectangular pulses. This is, to our knowledge, the first demonstration of shaped individual beamsplitter pulses preparing momentum superpositions being used to improve the contrast of an atom interferometer.

II. THEORETICAL SYSTEM AND OPTIMIZATION APPROACH

We consider an alkali atom undergoing stimulated Raman transitions between hyperfine levels, forming an effective 2-level system described using the basis states $|\mathrm{g}, \mathbf{p}\rangle$, and $|\mathrm{e}, \mathbf{p} + \hbar\mathbf{k}_L\rangle$ [50]. $\mathbf{p}$ is the atomic momentum and $\mathbf{k}_L$ represents the difference between the wave vectors of the two lasers, or 'effective' wave vector. The change in state under the action of a pulse of constant intensity and combined laser phase ϕ_L, acting for duration Δt, is described by a propagator

$$\hat{U} = \begin{pmatrix} C^* & -iS^* \\ -iS & C \end{pmatrix}, \tag{1}$$

where C and S are defined as [51]:

$$C \equiv \cos\left(\frac{\sqrt{\Omega_R^2+\delta^2}\Delta t}{2}\right) + i\left(\frac{\delta}{\sqrt{\Omega_R^2+\delta^2}}\right)\sin\left(\frac{\sqrt{\Omega_R^2+\delta^2}\Delta t}{2}\right) \quad (2)$$

$$S \equiv e^{i\phi_L}\left(\frac{\Omega_R}{\sqrt{\Omega_R^2+\delta^2}}\right)\sin\left(\frac{\sqrt{\Omega_R^2+\delta^2}\Delta t}{2}\right). \quad (3)$$

Ω_R is the two-photon Rabi frequency, and δ is the two-photon Raman detuning [1], which depends on atomic momentum and is assumed to be approximately constant for the duration of the pulses. This is often achieved by chirping the frequency difference of the Raman beams to account for the Doppler shift caused by gravitational acceleration [50].

Rectangular $\pi/2$ and π pulses are the building blocks of conventional interferometer sequences, and result from fixing the duration of a pulse with constant laser intensity and frequency such that the quantum state undergoes a $\pi/2$ or π rotation about an axis in the xy plane of the Bloch sphere [52]. Variations in the detuning (e.g. due to thermal motion) and Rabi frequency (e.g. due to beam intensity variation) across the atom cloud degrade the interferometer signal [53, 54]. In the NMR literature these errors are referred to as 'off-resonance' and 'pulse-length' errors respectively. If the individual pulses no longer perform the intended operations for each atom, the contrast of the interferometer fringes falls, their offset varies, and the inertial phase is modified [49, 51, 55]. Although the problem of intensity inhomogeneity in atom interferometry may be compensated by the use of collimated top-hat laser beams [56], our approach obtains tailored pulses that achieve mutual compensation of inhomogeneous coupling strengths and large Raman detunings without the need for additional optical elements.

We define our pulses in terms of multiple discrete time 'slices' where the combined Raman laser phase ϕ_L takes a different value for each equal timestep $\mathrm{d}t$ in the pulse. They are therefore described by profiles $\phi_L(t) = \{\phi_0, \phi_1, ..., \phi_N\}$, with a total duration τ_{pulse}. Although we could also choose to vary the pulse amplitude with time, for experimental simplicity we have considered pulses with constant amplitude profiles in this work. The laser phase forms our control parameter, and the action of a given pulse on our effective two-level system may be described by a sequence of pulse propagators $\hat{U}_n(\phi_n, \Omega_R, \delta, \mathrm{d}t)$. The action of a pulse is then a time-ordered product of propagators

$$\hat{U} = \hat{U}_N\hat{U}_{N-1}\ldots\hat{U}_n\ldots\hat{U}_1\hat{U}_0, \quad (4)$$

where the propagator for the nth timestep $\hat{U}_n$ takes the form of a rectangular pulse of fixed laser amplitude and phase acting for duration $\mathrm{d}t$ (Equation 1) [49, 51].

Optimal control theory finds the 'best' way to control the evolution of a system so as to maximize some fidelity or 'measure of performance'. Often, this fidelity is taken to be the accuracy with which initial states are driven to target states by the optimal modulation of available control fields. We employ the gradient ascent pulse engineering (GRAPE) [38] algorithm to design optimal pulses for our purposes. Given an initial guess for the pulse and a choice of pulse fidelity, GRAPE efficiently calculates the required propagator derivatives and recent improvements permit the use of a fast second order optimization, known as the limited-memory Broyden-Fletcher-Goldfarb-Shanno (L-BFGS) quasi-Newton method [41]. By defining an ensemble of systems with a distribution of atomic detunings (giving rise to 'off-resonance' errors) and variations in coupling strength (or, equivalently, 'pulse-length' errors), a robust pulse that maximizes the chosen fidelity over the ensemble may be obtained by averaging over the ensemble in the fidelity calculation. The length and number of timesteps are chosen at the outset and fixed when optimizing a pulse. Longer pulses can typically achieve higher terminal fidelities [39, 42]. The spin dynamics simulation software Spinach [40], and its optimal control module, was used to optimize pulses in this work.

III. MEASURES OF PULSE PERFORMANCE

The choice of pulse fidelity used in the optimization depends on the application, and requires a careful consideration of the experimental requirements. For example, we may write our pulse fidelity, $\mathcal{F}$, for a given atom as a function of the overlap of a chosen target state $|\psi_T\rangle$ with the final state after application of the pulse to our initial state $|\psi_0\rangle$: $\mathcal{F} = |\langle\psi_T|\hat{U}|\psi_0\rangle|^2$. This fidelity, when maximized, gives us a state-transfer or 'point-to-point' (PP) pulse [39]. Alternatively, the goal of the optimization may be to recreate a specific target propagator $\hat{U}_T$ and we consider the fidelity to be $\mathcal{F} = \frac{1}{2}\mathrm{Tr}(\hat{U}_T^\dagger\hat{U})$, yielding a so-called 'universal rotation' (UR) pulse [42]. Many other choices of pulse

fidelity are available, however, including those which map a range of initial states to different targets, and are not aimed at obtaining full universal rotations [46]. We discuss appropriate fidelity choices that maximize fringe visibility and minimize any unwanted spread in the inertial phase for two cases. Firstly, we consider a fidelity choice for pulses used to impart additional momentum in extended LMT interferometer sequences. Secondly, we present measures of performance for each pulse within a three-pulse 'Mach-Zehnder' interferometer sequence.

In LMT interferometers, the beamsplitter and mirror operations are extended by multiple 'augmentation' pulses with alternating effective wavevectors designed to swap the population of the internal states whilst imparting additional momentum [13, 14, 26]. In order to optimize an augmentation pulse for LMT interferometry, which we represent by the propagator $\hat{U}_{\mathrm{A}}$, it may be sufficient to consider the 'point-to-point' fidelity

$$\mathcal{F}_{\mathrm{A}} = |\langle \mathrm{e}|\, \hat{U}_{\mathrm{A}}\, |\mathrm{g}\rangle\, |^2 \tag{5}$$

without concern for the relative phase introduced between the two states. This is because, in LMT interferometers, the augmentation pulses appear in pairs within the extended pulse sequence [13, 14, 33] so that the interferometer phase introduced by each pulse is, to first order, cancelled out by that introduced by a subsequent one. Choosing to optimize a PP operation as opposed to a UR pulse effectively gives the GRAPE algorithm a larger target to shoot at, allowing impressive fidelity to be achieved with a modest pulse area.

In a three-pulse Mach-Zehnder interferometer sequence, $\pi/2$ and π pulses are applied to atoms initially in the state $|\mathrm{g}\rangle$ separated by equal 'dwell times' for which the fields are extinguished. Inertial effects such as rotations and accelerations imprint a relative phase Φ between the internal states at the end of the interferometer, which is mapped onto a population difference by the final $\pi/2$ pulse. The resulting excited state probability is

$$P_{\mathrm{e}} = \frac{1}{2}(\mathcal{A} - \mathcal{B}\cos(\Phi + \Delta\phi)) \tag{6}$$

where $\mathcal{A}$ and $\mathcal{B}$ are the offset and contrast of the interferometer fringes respectively. $\Delta\phi$ represents a fixed shift to the inertial phase used to scan the fringe pattern, and must be constant from atom to atom.

An optimal 3-pulse interferometer sequence, represented by propagators $\hat{U}_1, \hat{U}_2, \hat{U}_3$ should maximize the contrast $\mathcal{B}$, minimize any unwanted variation of/in the inertial phase, $\Delta\phi$, and fix the offset $\mathcal{A}$ for all atoms with the range of detunings and coupling strengths found in the atomic cloud. The optimal contrast and offset are achieved for all atoms if the following conditions on the 3 pulses are met:

$$|\langle \mathrm{e}|\hat{U}_{i=1,3}|\mathrm{g}\rangle\, |^2 = \frac{1}{2}, \tag{7a}$$

$$|\langle \mathrm{e}|\hat{U}_2|\mathrm{g}\rangle\, |^2 = 1. \tag{7b}$$

We interpret these conditions as requiring our beamsplitter pulses (pulses 1 and 3) to perform a 90° rotation of the quantum state about an axis in the xy plane of the Bloch sphere. Similarly, the optimal mirror pulse (pulse 2) must perform a robust 180° rotation of the quantum state. It is crucial for interferometry that the inertial phase Φ is not modified by a different amount for each atom as a result of the pulse sequence. This is equivalent to requiring the combined phase shift due to the pulse sequence, $\Delta\phi$, to be fixed or cancelled by the pulses for every atom, where

$$\begin{aligned}\Delta\phi = {} & \phi(\langle \mathrm{e}|\hat{U}_1|\mathrm{g}\rangle) - \phi(\langle \mathrm{g}|\hat{U}_1|\mathrm{g}\rangle) \\ & - 2\phi(\langle \mathrm{e}|\hat{U}_2|\mathrm{g}\rangle) \\ & + \phi(\langle \mathrm{g}|\hat{U}_3|\mathrm{g}\rangle) + \phi(\langle \mathrm{e}|\hat{U}_3|\mathrm{g}\rangle).\end{aligned} \tag{8}$$

We use the notation $\phi(\langle a|b\rangle)$ to indicate the argument of the overlap $\langle a|b\rangle$. If $\Delta\phi$ varies from atom to atom as it does with some pulses [49, 55], the resulting contrast after thermal averaging will be washed out. A careful choice of pulse fidelity for the beamsplitters and mirrors will lead to pulses that maximize interferometer contrast and minimize unwanted variation in the interferometer phase Φ from atom to atom.

Our first interferometer pulse $\hat{U}_1$ is designed to take atoms from the initial ground state, to a balanced superposition with well-defined phase on the equator of the Bloch sphere, $|\psi_T\rangle = (|\mathrm{g}\rangle + |\mathrm{e}\rangle)/\sqrt{2}$. This means our beamsplitter fidelity, $\mathcal{F}_1$, can be written as

$$\mathcal{F}_1 = |\langle \psi_T|\, \hat{U}_1\, |\mathrm{g}\rangle\, |^2, \tag{9}$$

yielding a PP 90° pulse. This choice of fidelity, if maximized, results in a beamsplitter which satisfies the conditions $|\langle \mathrm{e}|\hat{U}_1|\mathrm{g}\rangle\, |^2 = 1/2$ and $\phi(\langle \mathrm{e}|\hat{U}_1|\mathrm{g}\rangle) - \phi(\langle \mathrm{g}|\hat{U}_1|\mathrm{g}\rangle) = 0$.

The mirror pulse, $\hat{U}_2$, acting after the first period of free evolution, is designed to swap the internal states, but introduce no relative phase between them, satisfying conditions $|\langle e|\hat{U}_2|g\rangle|^2 = 1$ and $\phi(\langle e|\hat{U}_2|g\rangle) =$ constant. This pulse is designed to perform a π rotation on the Bloch sphere about a fixed axis in the xy plane. We can therefore consider the mirror pulse fidelity to be a measure of how close our pulse propagator is to that for an ideal π rotation, $\hat{U}_\pi$, and optimize the UR 180° fidelity

$$\mathcal{F}_2 = \frac{1}{2}\mathrm{Tr}(\hat{U}_\pi^\dagger \hat{U}_2) \tag{10}$$

[42, 49]. Designing the mirror pulse as a universal rotation means that variations to the inertial phase Φ that vary with δ and Ω_R are minimized. We also note that if the pulse profile of the mirror pulse is made to be odd or antisymmetric about its temporal midpoint, then any modification to the inertial phase will be constant for all δ and Ω_R. This follows from the fact that pulses with this symmetry fix the axis of rotation to the xz plane of the Bloch sphere for all resonance offsets, a property known in the NMR literature [42, 57, 58]. Antisymmetric UR 180° pulses may be constructed by first optimizing a single PP 90° pulse and following the steps outlined by Luy *et al.* [59].

Finally, the third pulse is designed to accurately map the relative phase acquired between the two internal states at the end of the second dwell time, onto a difference in atomic population. This pulse does not need to be a universal 90° rotation, as only the z-component of the final Bloch vector matters when measuring the excited state population at the end of the interferometer. The action of this pulse can be thought of as a phase sensitive $\pi/2$ rotation, and may be obtained by taking the pulse profile for the first pulse $\phi_L(t)$, and reversing it in time about the temporal mid-point and inverting the pulse profile to obtain $-\phi(\tau - t)$. This "flip-reverse" operation relies on the symmetry properties of spin-$\frac{1}{2}$ propagators [60, 61]. The result is a pulse which satisfies $|\langle e|\hat{U}_3|g\rangle|^2 = 1/2$ but which has $\phi(\langle g|\hat{U}_3|g\rangle) + \phi(\langle e|\hat{U}_3|g\rangle) = -\phi(\langle e|\hat{U}_1|g\rangle) + \phi(\langle g|\hat{U}_1|g\rangle) + \pi$, thus satisfying the condition on $\Delta\phi$. Optimizing the 3-pulse interferometer with these symmetry constraints (the final pulse has the time-reversed and inverted profile of the first beamsplitter) minimizes the unwanted modification to the inertial phase term Φ and maximizes the contrast of resulting fringes.

IV. RESULTS OF OPTIMIZATIONS

Figure 1 shows pulses obtained using GRAPE optimizing a PP 180° inversion pulse, a PP 90° beamsplitter pulse, and an antisymmetric UR 180° mirror pulse. The duration of each pulse, the number of timesteps, and the initial guess for the pulse, are chosen in advance. The pulse duration and timestep number are chosen so that a sufficiently high terminal fidelity (0.99) can be achieved. The chosen fidelity is averaged over an ensemble to obtain robust solutions. The ensembles are defined in terms of a sample of off-resonance and pulse-length errors. The sample of off-resonance errors is taken to reflect the variation in detuning caused by the momentum distribution of the atoms at a given temperature along the Raman beam axis, which we assume to follow a Maxwell-Boltzmann distribution. Choosing to optimize over an ensemble representing a larger temperature will result in a pulse that is robust over a larger range of detunings, and will therefore still have high fidelity if the temperature of the atomic ensemble is reduced.

Taking the beamsplitter and mirror pulses shown in Figure 1, we can simulate how the resulting interferometer contrast varies with detuning and variation in coupling strength. Figure 2 compares the simulated interferometer contrast $\mathcal{B}$ obtained with our "flip-reverse" GRAPE sequence, and the standard rectangular $\pi/2 - \pi - \pi/2$ sequence, over a range of pulse-length errors and detunings. We also show the simulated contrast following a sequence composed of rectangular pulses, but where the central π pulse is replaced by an efficient state-transfer PP composite pulse known as WALTZ [14, 33, 62]. We find that the interferometer contrast with our optimized GRAPE pulses is more resilient to variations in detuning and coupling strength. For example, Figure 2 shows that the "flip-reverse" sequence is expected to maintain an interferometer contrast above 90% for a range of detuning which is 4.6 times greater than that for a sequence of rectangular pulses, and 1.3 times greater than when employing the WALTZ composite pulse.

Although WALTZ is able to increase the contrast for a range of atomic velocities and variations in Rabi frequency, the resulting interferometer phase Φ exhibits a large unwanted variation as a function of the Raman detuning, as shown in Figure 3. This is because WALTZ is a point-to-point transformation, and therefore not suitable to replace the central mirror pulse in an atom interferometer. If atoms with different velocities obtain different interferometric phases following a pulse sequence, the interference fringes will be washed out following thermal averaging [49, 55]. However, Figure 3 also shows that the interferometer phase following our antisymmetric "flip-reverse" sequence is expected to be insensitive to variations in Raman detuning, emphasising the potential applicability of robust antisymmetric pulse sequences.

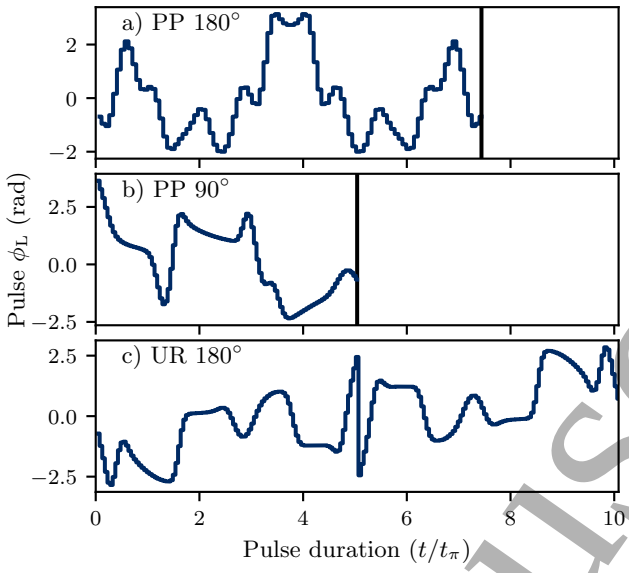

FIG. 1. Optimization results for an individual LMT augmentation pulse $\mathcal{F}_A$ (a), a beamsplitter pulse $\mathcal{F}_1$ (b), and an antisymmetric mirror pulse $\mathcal{F}_2$ (c). The pulse profiles are plotted against time as a fraction of the duration of a rectangular π pulse, t_π. Each optimization was continued until fidelities greater than 0.99 were reached. Each pulse was optimized for an ensemble of atoms with a temperature of 120 μK and a range of coupling strengths of $\pm$ 10% Ω_{eff}.

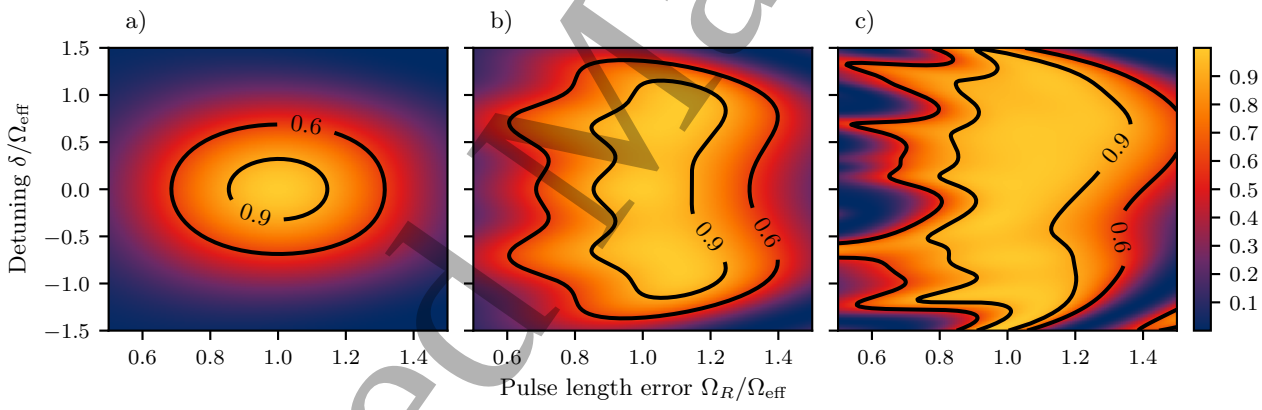

FIG. 2. Simulated 3-pulse interferometer contrast $\mathcal{B}$ for (a) standard rectangular $\pi/2 - \pi - \pi/2$ sequence, (b) rectangular sequence where the π pulse is replaced by the WALTZ composite pulse [62], and (c) our GRAPE "flip-reverse" sequence, computed for a range of off-resonance and pulse-length errors. Contours are at 0.6, and 0.9 respectively. The effective Rabi frequency Ω_{eff} and π pulse duration t_π are defined by requiring that $\Omega_{\text{eff}} t_\pi = \pi$. The robustness of the GRAPE sequence to these inhomogeneities is shown by the increased area of high contrast centered on resonance.

V. EXPERIMENTAL PROCEDURE

We have implemented our pulses in our experimental setup, a description of which can be found in previous work [33, 63], but we take a moment here to outline the most salient points.

We realize our pulses on a thermal cloud of $\sim 10^7$ ^{85}Rb, released from a 3-D magneto-optical trap (MOT), cooled in an optical molasses for ~ 5 ms and optically pumped into the $5S_{1/2}, F = 2$ state with a distribution over the five m_F sublevels which, as the pumping is performed with the MOT light along all axes, is assumed to be uniform [33].

The cloud temperature is tuned by adjusting the intensity of the cooling light during the optical molasses and is measured by performing Raman Doppler spectroscopy with the Raman beams at low power [64]. The temperature can be adjusted in the range of $20 - 200$ μK and, combined with the multiple Rabi frequencies due to the different coupling strengths of the five m_F levels present in the sample, provides an inhomogeneous system with which to

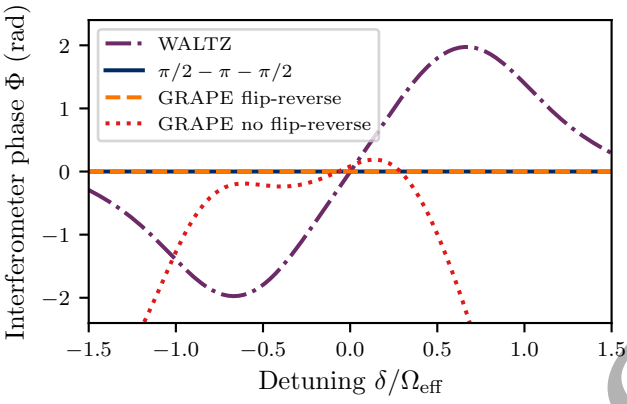

FIG. 3. Simulated interferometer phase, Φ, as a function of the Raman detuning for different interferometer sequences. The interferometer phase following the rectangular $\pi/2-\pi-\pi/2$ sequence does not exhibit variation with the Raman detuning, but if the π pulse is replaced by a PP pulse such as the composite WALTZ pulse there is an unwanted variation in Φ. This variation of Φ with δ means that the ensemble averaged interference is washed out and contrast is reduced [49, 55]. Following our antisymmetric "flip-reverse" sequence, Φ has no dependence on the Raman detuning, highlighting the applicability of interferometer sequences designed with antisymmetry. However, if the final beamsplitter is simply the same as the first and no "flip-reverse" procedure is applied, the result is a large variation in Φ.

explore the performance of pulses designed to provide robustness against the resulting off-resonance and pulse-length errors.

Interferometry pulses are realised via horizontal, counter-propagating beams with orthogonal linear polarizations that interact with the released cloud to drive two-photon Raman transitions on the D2 line between the $F = 2$ and $F = 3$ hyperfine ground states (states $|g\rangle$ and $|e\rangle$ respectively). Both laser fields are ~ 10 GHz detuned from single-photon resonance with the intermediate $F' = 2, 3$ states of the $5P_{3/2}$ manifold, thus allowing our atoms to be modelled as effective two-level systems [1], and the polarization arrangement removes the m_F dependence of the light shift [33].

One beam is formed from the first diffracted order of a 310MHz acousto-optic modulator (AOM) and the other from the carrier suppressed output of a 2.7GHz electro-optic modulator (EOM). The modulator frequencies sum to the hyperfine splitting between the ground states plus a detuning δ applied to the carrier frequency of the EOM RF signal. The beams are combined on a single AOM to shutter the interaction light on and off with a rise-time of ~ 100 ns before being separated by polarization and delivered to the atom cloud through separate polarization-maintaining fibers.

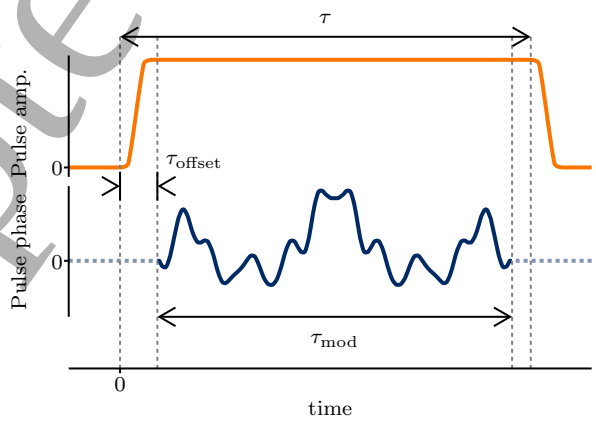

FIG. 4. Illustration, not to scale, of the timing parameters optimized to realize optimal inversion pulses. The Raman light (top) is turned on at $t = 0$, and off again at $t = \tau$ by an AOM with a rise-time of ~ 100 ns. The sample rate of the AWG controlling the phase (bottom) is adjusted to set the total duration of the phase waveform $\tau_{\rm mod}$, and this is adjusted together with the trigger delay $\tau_{\rm offset}$ to achieve the optimal peak transfer when τ is scanned. When the phase waveform has finished, the phase is maintained at its final value ϕ_N.

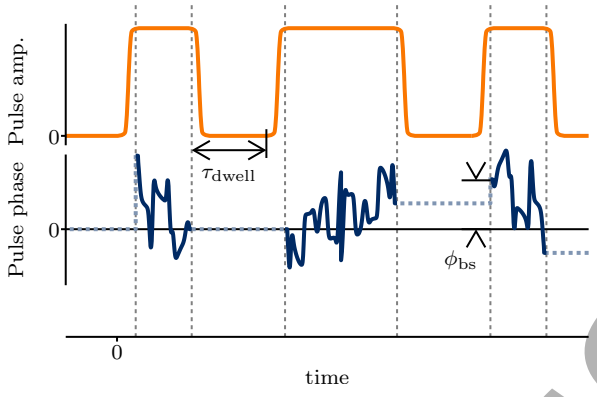

FIG. 5. Illustration, not to scale, of an optimized interferometer sequence. Three pulses, as depicted in figure 4, are combined, with a time τ_{dwell} between the light of one pulse turning off and the subsequent pulse turning on. Fringes are measured by measuring the fraction of atoms in the excited state at the end of the sequence as a function of a phase offset ϕ_{bs} applied to the phase sequence for the final beamsplitter pulse.

The phase of the RF signal driving the EOM is modulated with a Miteq SDM0104LC1CDQ I&Q modulator, the I and Q inputs of which are controlled by the dual outputs of a Keysight 33612A arbitrary waveform generator (AWG). To realize a phase sequence $\phi_n, n = 1, 2, ..., N$, the outputs are programmed with the waveforms $I_n = \sin(\phi_n)$ and $Q_n = \cos(\phi_n)$ and are configured to hold the final phase value ϕ_N until a hardware trigger is received and the waveforms are played at a sample rate that is adjusted to set the total duration of the modulation τ_{mod} [65].

As in our previous work, the fraction of atoms P_e in the excited state following a Raman pulse is determined from a normalized measurement of the amplitude of the cloud fluorescence upon illumination with the MOT cooling beam in a read-out procedure that is fully detailed in [66]. By concurrently triggering the phase modulation AWG and the AOM that shutters the Raman beams to initiate a pulse, then measuring P_e once the AOM shutter has been turned off again after a variable time τ, we can track the temporal evolution of the atomic state during a phase sequence. The hardware trigger delay and sample rate of the AWG are adjusted in order to vary the start time τ_{offset} and duration τ_{mod} of the phase waveform respectively (Figure 4) and maximize the peak excited fraction in these temporal scans.

Having chosen the experimental pulse timings such that the fidelity is maximized at a single value of the Raman detuning δ, set to the centre of the light-shifted resonance determined from the spectral profile of a rectangular π-pulse, a spectral profile can be measured by measuring P_e upon completion of the pulse at a range of detuning values.

Multiple pulses can be performed sequentially, separated by periods of free evolution τ_{dwell}, in order to test optimized interferometer sequences as illustrated in Figure 5. The interferometer contrast is then tested by varying a phase offset ϕ_{bs} applied to the phase sequence for the final beamsplitter pulse between 0 to 4π and fitting a sinusoidal function to the resulting fringes in P_e.

VI. RESULTS: LMT INVERSION PULSES

We have designed a population inversion pulse using GRAPE that maximizes the transfer of atoms initially in the state $|\mathrm{g}\rangle$ to the state $|\mathrm{e}\rangle$ for a cloud with a temperature of 120 μK and a large variation in Rabi frequency of $\pm 10\%$ Ω_{eff}.

The pulse duration was chosen to be 12 μs for a Rabi frequency of 310 kHz, making it 7.4 times longer than a rectangular π-pulse, and allowing for a high terminal optimization fidelity. This pulse had 100 timesteps and the algorithm converged to the symmetric waveform shown in Figures 1 and 6 when optimizing the point-to-point fidelity $\mathcal{F}_{\mathrm{A}}$ with a penalty term added, proportional to the difference between adjacent pulse steps, to enforce waveform smoothness [43]. We found that increasing the number of timesteps in this pulse led only to a negligible increase in fidelity.

The temporal profile, after optimizing τ_{offset}, is shown in Figure 6, showing a peak in the excited fraction P_e at the end of the phase sequence, represented by the vertical dashed line, after which damped Rabi oscillations are evident as the phase is kept constant.

We find that optimized pulses demonstrate a considerable resilience to variations in the trigger delay τ_{offset}, and can be started as much as a quarter of a π-pulse duration after the light is turned on with little change to the peak

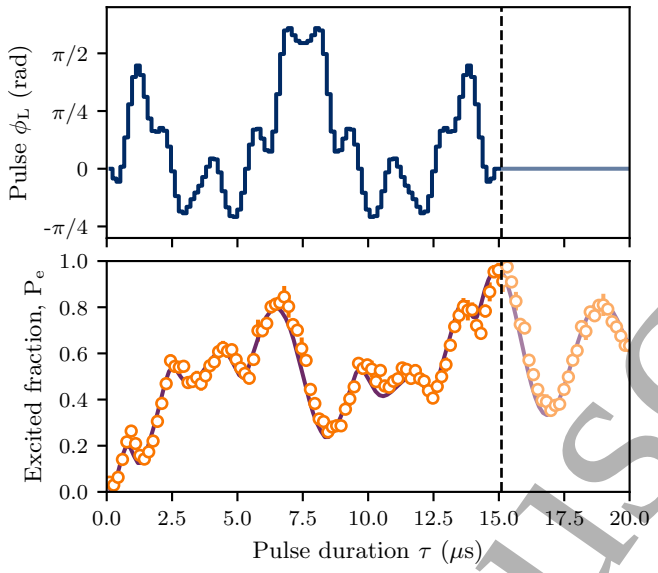

FIG. 6. *Above*: Optimal state transfer pulse designed using GRAPE to transfer atoms between levels $|g\rangle$ and $|e\rangle$. *Below*: Measured fraction (circles) of atoms in the excited state P_e after the Raman light is extinguished at various times during a pulse. The solid line is a theoretical curve produced by the model from [33], in which the two-level Hamiltonian is numerically integrated over the range of detunings and coupling strengths present in a thermal cloud of ^{85}Rb atoms, and assumes that the light reaches full intensity instantaneously and concurrently with the start of the phase modulation. Excellent agreement is observed for a simulated temperature of 35 μK.

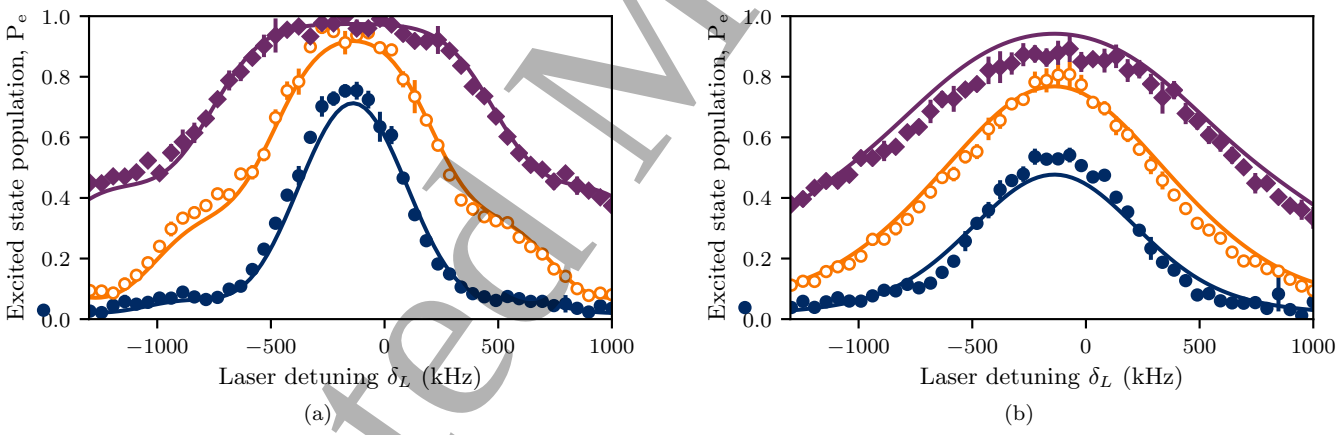

FIG. 7. Fraction of atoms transferred to the excited state P_e as a function of laser detuning δ_L in (a) a 35 μK atom cloud and a (b) 150 μK cloud. Data are shown for our GRAPE pulse (diamonds), the WALTZ pulse (empty circles) and a rectangular π-pulse (filled circles). The effective Rabi frequency was 270 kHz. Solid lines show theory curves produced from the model used by Dunning *et al.* [33], which assumes a Maxwell-Boltzmann atomic velocity distribution. The offset of the peaks from $\delta_L = 0$ is due to the light shift.

transfer.

The highest excited fraction for all pulses is achieved when the light is kept on for slightly longer than the phase sequence, with $\tau > \tau_{\text{mod}}$ by ~ 200 ns. The AOM rise-time is not factored into the optimization process and this is the only effect of it that we observe experimentally, with the temporal data being well fitted by a numerical model that assumes the light reaches full intensity instantaneously at the start of the phase sequence as shown in Figure 6.

To demonstrate the potential of this GRAPE pulse for augmenting LMT beamsplitters, we compare its performance with the WALTZ composite pulse, the best composite Raman pulse previously used for LMT interferometry [14], and the standard rectangular π pulse over a range of detunings δ.

In a sub-Doppler cooled cloud of 35 μK, GRAPE and WALTZ pulses achieve close to 99.8(3)% and 96(2)% transfer

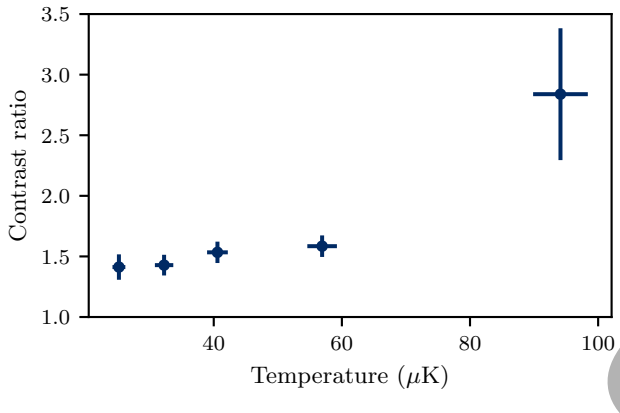

FIG. 8. Ratio of contrasts obtained by fitting sinusoidal functions to fringes obtained from optimized "flip-reversed" GRAPE and rectangular interferometer sequences for a range of cloud temperatures. GRAPE consistently improves the interferometer contrast with a significant 2.8(6) times improvement at the highest cloud temperature of 94(4) μK where temperature and not laser phase noise is the dominant source of contrast loss.

respectively about the light-shifted resonance, while a rectangular π-pulse achieves just 75(3)%. This is shown in Figure 7, where the broadband nature of the GRAPE pulse is evident, while the fidelity of the WALTZ pulse drops below 90% when detuned 100 kHz from resonance, the GRAPE pulse can be detuned by 380 kHz for the same fidelity. This broad spectral profile is a signature of a good LMT augmentation pulse, which must work equally well for atoms that have received a large number of recoil kicks [14].

In a cloud with a temperature much closer to the Doppler cooling limit ~ 150 μK, for which the peak transfer of a rectangular π-pulse is just 54(2)%, the broader spectral width of the WALTZ and GRAPE pulses results in more efficient state transfer on resonance. This is also shown in Figure 7, where the GRAPE pulse achieves 89(4)% transfer on resonance compared with 81(4)% for WALTZ.

VII. RESULTS: MACH-ZEHNDER INTERFEROMETER

Using fidelities for optimal beamsplitter and mirror pulses ($\mathcal{F}_1$ and $\mathcal{F}_2$) we optimized all three pulses of the Mach-Zehnder interferometer sequence for an atomic sample with a temperature of 120 μK and a coupling strength variation of $\pm 10\%$ Ω_{eff}. The resulting pulse profiles are shown in Figure 1 (b, c). The phase sequence of the final pulse was taken to be the inverted and time-reversed profile of the first according to the design procedure outlined in section III. As illustrated in Figure 2, we expect our optimal Mach-Zehnder sequence of pulses is capable of maintaining a higher contrast than conventional rectangular pulses despite significant variations in detuning and Rabi-frequency in the atomic cloud.

We have started to test these three-pulse interferometer sequences in our experimental apparatus, comparing the performance with that obtained using a sequence of conventional rectangular $\pi/2$ and π pulses. Interferometer fringes are obtained by scanning the phase offset ϕ_{bs} applied to the final pulse in the sequence. The dwell time between pulses is limited, at present, to 100 μs by suspected phase noise between the counter-propagating beams that also limits the overall contrast. The initial results are promising, and the relative improvement in contrast provided by the GRAPE-optimized sequence as the cloud temperature is varied is shown in Figure 8. GRAPE improved the contrast of the fringes at all temperatures investigated and, in a hot 94(4) μK sample where the contrast loss is dominated by atomic temperature and not the laser phase noise, nearly a threefold enhancement is observed, the fringes for which are shown in Figure 9. This enhancement is also apparent in the uncertainties in the phases of the fitted sinusoids. At 94(4) μK the average uncertainty in the fitted phase due to the GRAPE sequence was a factor of 2.9 smaller than the uncertainty in the fitted phase from the rectangular pulse sequence.

Applying the "flip-reverse" operation to obtain the final beamsplitter is necessary to observe an increase in contrast with GRAPE. For example, at a temperature of $\sim$25 μK, the contrast following the full antisymmetric "flip-reverse" sequence depicted in Figure 5 was higher by a factor of 2 than the contrast following a sequence which was in all respects identical but where the flip reversal procedure was not applied to the final beamsplitter. This sequence leads to a large variation of the interferometer phase with detuning (shown in Figure 3), thereby causing atoms with different velocities to exit the interferometer with different phases and the interference to wash out when the signal is averaged over the ensemble.

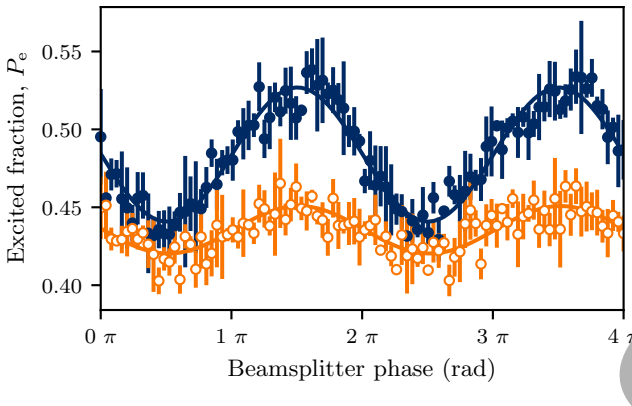

FIG. 9. Interferometer fringes obtained at 94(4) μK for rectangular pulses (empty circles) and the optimized GRAPE sequence (filled circles). The GRAPE sequence improved the contrast of the fringes by a factor of 2.8(6). The average or, 'effective' Rabi frequency was approximately 420 kHz, and was determined empirically from the optimal duration of a rectangular π pulse. We attribute the slight deviation of the fringes from a sinusoidal form to a small non-linearity in the response of the I&Q modulator.

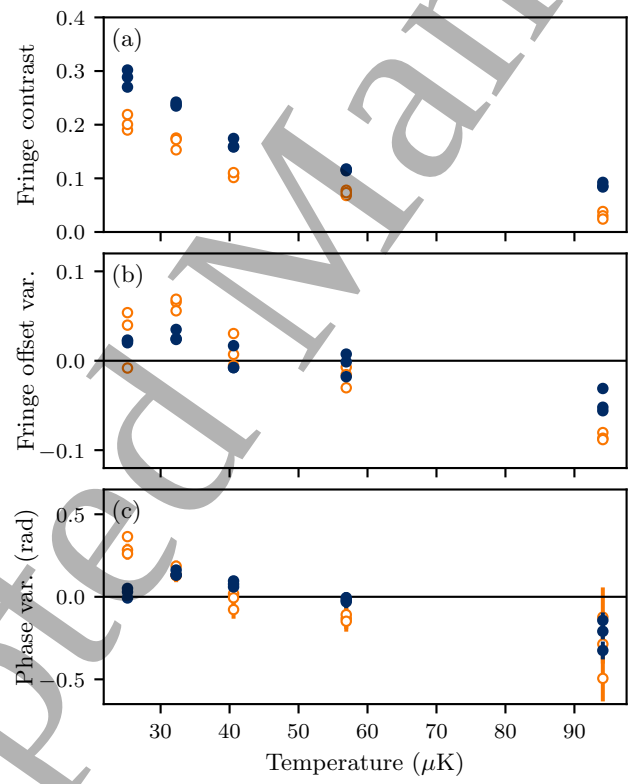

FIG. 10. Variation in fitting parameters for sinusoidal functions fitted to fringes obtained from GRAPE optimized (filled circles) and rectangular (empty circles) interferometer sequences at a range of cloud temperatures. (a) shows the fringe contrast $\mathcal{B}$, while (b) and (c) show the shifts in the fringe offset $2\mathcal{A}$ and phase from their respective mean values. The GRAPE interferometer has consistently higher contrast than the rectangular counterpart, and exhibits less variation in both fringe offset and phase. Temperature error bars are omitted for clarity, but are the same as in Figure 8. The vertical error bars represent the fitting uncertainty of the sinusoidal curves to each experimental run; for the contrast and fringe offset measurements these have magnitudes $\sim \pm 0.005$, while the phase becomes more uncertain with reduced contrast. Consequently, at 25 μK and 94 μK the phase variation errors for GRAPE pulses are $\sim \pm 0.04$ rad and $\sim \pm 0.1$ rad respectively, while those for rectangular pulses are $\sim \pm 0.07$ rad and $\sim \pm 0.3$ rad. Data points for several experimental runs at each temperature are shown, and their vertical spread gives indication of the variation of each parameter over longer timescales measured in tens of minutes.

Some experimental evidence suggests that GRAPE sequences are less susceptible to drifts in offset and phase of the interferometer fringes. The variation of the fringe offsets and phases from their respective means for a range of temperatures for GRAPE and rectangular interferometers are shown in Figure 10(b) and 10(c), and we hope to explore this aspect more systematically in future work. In particular, there appears to be a systematic shift in the interferometer phase as the temperature is increased that we do not fully understand, but could possibly be caused by an offset of the laser detuning from the centre of the atomic momentum distribution [67]. It is notable that the GRAPE interferometer appears less susceptible to this shift.

Another route of inquiry will be to explain why the increase in contrast is quite so large only when employing a fully optimised pulse sequence. While the mirror pulse, with its increased Doppler sensitivity, should be the dominant source of contrast loss in a Mach-Zehnder interferometer [49], only a slight enhancement was observed when just this pulse was replaced. To see significant improvement from a fully optimized sequence, maintaining the overall anti-symmetry in a "flip-reversed" configuration proved necessary. When this constraint was met, the contrast improvement far exceeded that of replacing just the mirror, or indeed the beamsplitters, in isolation.

VIII. CONCLUSION

We have presented the design and experimental implementation of optimal Raman pulses that obtain significant improvements in fidelity compared with conventional pulses. We have used optimal control to design Raman pulses that achieve robust population inversion in the presence of variations in the atom-laser coupling strength and detuning, designed to improve the contrast of LMT interferometers. We have also outlined and demonstrated a design for optimal pulses that improve the contrast of the three-pulse Mach-Zehnder sequence. We expect such optimal pulse sequences to have applications in improving the sensitivity and robustness of atom interferometric sensors operating in non-ideal environments, relaxing the requirement for low atomic temperatures and potentially reducing their susceptibility to drifts in the signal phase and offset.

Specifically, we have presented a 'point-to-point' inversion pulse that achieves 99.8(3)% transfer between hyperfine ground states in a thermal cloud of ^{85}Rb atoms. Our pulse has a broad spectral profile making it a good candidate for an augmentation pulse in LMT interferometry where a large velocity acceptance is required. The best results of Raman LMT interferometers to date have been achieved with adiabatic augmentation pulses [26, 27], but optimal control pulses such as this have the potential to realize similarly robust transfer with significant reductions in pulse duration [39, 68].

Furthermore, we have detailed a strategy for optimizing 3-pulse Mach-Zehnder type interferometer sequences in which optimized beamsplitter and mirror pulses are combined in a "flip-reversed" configuration to maximize the contrast of interferometer fringes where the phase of atomic superpositions is important. We have shown up to a threefold contrast improvement in a proof-of-principle interferometer with hot 94(4) μK atoms, although our current investigations have been limited by experimental phase noise. We emphasize that although our interferometer dwell time is limited to 100 μs at present, our technique can mitigate errors in coupling strength and detuning that are often present in more sensitive interferometers, for example those which increase the scale factor by increasing the momentum splitting of the diffracting wave packets [14, 26].

Future work will extend our experimental study of optimized interferometer sequences to test their efficacy and robustness when experimental noise is no longer such a limiting constraint. The excellent agreement between experiment and theory over the timescale of a single pulse suggests that, at present, the experiment is not limited by the mapping of the phase modulation waveforms and that the phase noise is only significant over longer timescales. We therefore suspect lower frequency, mechanical noise to be the dominant factor and are working to minimize this.

We are also exploring alternative fidelity measures and ways to optimize all pulses concurrently within interferometer sequences, along with considering — both computationally and analytically — how to use the framework of optimal control to engineer robustness to other factors such as laser phase noise in atom interferometers.

ACKNOWLEDGMENTS

The authors are grateful to David Elcock for his contributions to the stabilization and characterization of the optical and RF apparatus. This work was supported by the UK Engineering and Physical Sciences Research Council (Grant Nos. EP/M013294/1 and EP/L015382/1), and by Dstl (Grant Nos. DSTLX-1000091758 and DSTLX-1000097855).

Jack Saywell and Max Carey contributed equally to this work.

[1] P. Berman, ed., *Atom Interferometry* (Academic Press, 1997).
[2] B. Canuel, F. Leduc, D. Holleville, A. Gauguet, J. Fils, A. Virdis, A. Clairon, N. Dimarcq, C. J. Bordé, A. Landragin, and P. Bouyer, Phys. Rev. Lett. **97**, 010402 (2006).
[3] S. M. Dickerson, J. M. Hogan, A. Sugarbaker, D. M. S. Johnson, and M. A. Kasevich, Phys. Rev. Lett. **111**, 083001 (2013).
[4] B. Barrett, R. Geiger, I. Dutta, M. Meunier, B. Canuel, A. Gauguet, P. Bouyer, and A. Landragin, Comptes Rendus Physique **15**, 875 (2014).
[5] P. Cheiney, L. Fouché, S. Templier, F. Napolitano, B. Battelier, P. Bouyer, and B. Barrett, Physical Review Applied **10**, 034030 (2018).
[6] S. Dimopoulos, P. W. Graham, J. M. Hogan, M. A. Kasevich, and S. Rajendran, Phys. Lett. B **678**, 37 (2009).
[7] P. W. Graham, J. M. Hogan, M. A. Kasevich, and S. Rajendran, Phys. Rev. Lett. **110**, 171102 (2013).
[8] A. Wicht, J. M. Hensley, E. Sarajlic, and S. Chu, Physica Scripta **T102**, 82 (2002).
[9] M. Cadoret, E. de Mirandes, P. Cladé, S. Guellati-Khélifa, C. Schwob, F. Nez, L. Julien, and F. Biraben, Physical Review Letters **101**, 230801 (2008).
[10] G. Rosi, F. Sorrentino, L. Cacciapuoti, M. Prevedelli, and G. M. Tino, Nature **510**, 518 (2014).
[11] P. Hamilton, M. Jaffe, P. Haslinger, Q. Simmons, H. Muller, and J. Khoury, Science **349**, 849 (2015).
[12] C. Burrage, E. J. Copeland, and E. Hinds, Journal of Cosmology and Astroparticle Physics **2015**, 042 (2015).
[13] J. M. McGuirk, M. J. Snadden, and M. A. Kasevich, Phys. Rev. Lett. **85**, 4498 (2000).
[14] D. L. Butts, K. Kotru, J. M. Kinast, A. M. Radojevic, B. P. Timmons, and R. E. Stoner, Journal of the Optical Society of America B **30**, 922 (2013).
[15] S. S. Szigeti, J. E. Debs, J. J. Hope, N. P. Robins, and J. D. Close, New Journal of Physics **14**, 023009 (2012).
[16] T. Kovachy, P. Asenbaum, C. Overstreet, C. Donnelly, S. Dickerson, A. Sugarbaker, J. Hogan, and M. Kasevich, Nature **528**, 530 (2015).
[17] P. Cladé, S. Guellati-Khélifa, F. Nez, and F. Biraben, Physical Review Letters **102**, 240402 (2009).
[18] H. Müller, S.-w. Chiow, S. Herrmann, and S. Chu, Physical Review Letters **102**, 240403 (2009).
[19] G. D. McDonald, C. C. N. Kuhn, S. Bennetts, J. E. Debs, K. S. Hardman, M. Johnsson, J. D. Close, and N. P. Robins, Phys. Rev. A **88**, 053620 (2013).
[20] H. Müller, S. W. Chiow, Q. Long, S. Herrmann, and S. Chu, Phys. Rev. Lett. **100**, 180405 (2008).
[21] P. A. Altin, M. T. Johnsson, V. Negnevitsky, G. R. Dennis, R. P. Anderson, J. E. Debs, S. S. Szigeti, K. S. Hardman, S. Bennetts, G. D. McDonald, L. D. Turner, J. D. Close, and N. P. Robins, New Journal of Physics **15**, 023009 (2013).
[22] T. Kovachy, P. Asenbaum, C. Overstreet, C. A. Donnelly, S. M. Dickerson, A. Sugarbaker, J. M. Hogan, and M. A. Kasevich, Nature **528**, 530 (2015).
[23] J. S. Melinger, S. R. Gandhi, A. Hariharan, D. Goswami, and W. S. Warren, The Journal of Chemical Physics **101**, 6439 (1994).
[24] M. Garwood and L. DelaBarre, Journal of Magnetic Resonance **153**, 155 (2001).
[25] T. Kovachy, S.-w. Chiow, and M. A. Kasevich, Physical Review A **86**, 011606 (2012).
[26] K. Kotru, D. L. Butts, J. M. Kinast, and R. E. Stoner, Phys. Rev. Lett. **115**, 103001 (2015).
[27] M. Jaffe, V. Xu, P. Haslinger, H. Müller, and P. Hamilton, Phys. Rev. Lett. **121**, 040402 (2018).
[28] J. Bateman and T. Freegarde, Phys. Rev. A **76**, 013416 (2007).
[29] M. H. Levitt and R. Freeman, Journal of Magnetic Resonance (1969) **43**, 65 (1981).
[30] M. H. Levitt, Progress in Nuclear Magnetic Resonance Spectroscopy **18**, 61 (1986).
[31] R. Freeman, Progress in Nuclear Magnetic Resonance Spectroscopy **32**, 59 (1998).
[32] S. McDonald and W. S. Warren, Concepts in Magnetic Resonance **3**, 55 (1991).
[33] A. Dunning, R. Gregory, J. Bateman, N. Cooper, M. Himsworth, J. A. Jones, and T. Freegarde, Phys. Rev. A **90**, 033608 (2014).
[34] W. S. Warren, H. Rabitz, and M. Dahleh, Science **259**, 1581 (1993).
[35] C. Brif, R. Chakrabarti, and H. Rabitz, New Journal of Physics **12**, 075008 (2010).
[36] S. J. Glaser, U. Boscain, T. Calarco, C. P. Koch, W. Köckenberger, R. Kosloff, I. Kuprov, B. Luy, S. Schirmer, T. Schulte-Herbrüggen, D. Sugny, and F. K. Wilhelm, European Physical Journal D **69**, 279 (2015).
[37] T. E. Skinner, T. O. Reiss, B. Luy, N. Khaneja, and S. J. Glaser, Journal of Magnetic Resonance **163**, 8 (2003).
[38] N. Khaneja, T. Reiss, C. Kehlet, T. Schulte-Herbrüggen, and S. J. Glaser, Journal of Magnetic Resonance **172**, 296 (2005).
[39] K. Kobzar, T. E. Skinner, N. Khaneja, S. J. Glaser, and B. Luy, Journal of Magnetic Resonance **170**, 236 (2004).
[40] H. J. Hogben, M. Krzystyniak, G. T. P. Charnock, P. J. Hore, and I. Kuprov, Journal of Magnetic Resonance **208**, 179 (2011).
[41] P. De Fouquieres, S. G. Schirmer, S. J. Glaser, and I. Kuprov, Journal of Magnetic Resonance **212**, 412 (2011).
[42] K. Kobzar, S. Ehni, T. E. Skinner, S. J. Glaser, and B. Luy, Journal of Magnetic Resonance **225**, 142 (2012).
[43] D. L. Goodwin and I. Kuprov, J. Chem. Phys. **144**, 204107 (2016).
[44] T. Nöbauer, A. Angerer, B. Bartels, M. Trupke, S. Rotter, J. Schmiedmayer, F. Mintert, and J. Majer, Phys. Rev. Lett.

115, 190801 (2015).
[45] C. P. Koch, J. P. Palao, R. Kosloff, and F. Masnou-Seeuws, Phys. Rev. A **70**, 013402 (2004).
[46] S. van Frank, A. Negretti, T. Berrada, R. Bücker, S. Montangero, J.-F. Schaff, T. Schumm, T. Calarco, and J. Schmiedmayer, Nature Communications **5** (2014).
[47] G. Jäger, D. M. Reich, M. H. Goerz, C. P. Koch, and U. Hohenester, Phys. Rev. A **90**, 033628 (2014).
[48] P. B. Wigley, P. J. Everitt, A. van den Hengel, J. W. Bastian, M. A. Sooriyabandara, G. D. McDonald, K. S. Hardman, C. D. Quinlivan, P. Manju, C. C. N. Kuhn, I. R. Petersen, A. N. Luiten, J. J. Hope, N. P. Robins, and M. R. Hush, Scientific Reports **6**, 25890 (2016).
[49] J. C. Saywell, I. Kuprov, D. Goodwin, M. Carey, and T. Freegarde, Phys. Rev. A **98**, 023625 (2018).
[50] M. Kasevich and S. Chu, Phys. Rev. Lett. **67**, 181 (1991).
[51] R. Stoner, D. Butts, J. Kinast, and B. Timmons, Journal of the Optical Society of America B **28**, 2418 (2011).
[52] R. P. Feynman, F. L. Vernon, and R. W. Hellwarth, J. Appl. Phys. **28**, 49 (1957).
[53] A. Gauguet, B. Canuel, T. Lévèque, W. Chaibi, and A. Landragin, Phys. Rev. A **80**, 063604 (2009).
[54] G. W. Hoth, B. Pelle, S. Riedl, J. Kitching, and E. A. Donley, Applied Physics Letters **109**, 071113 (2016).
[55] Y. Luo, S. Yan, Q. Hu, A. Jia, C. Wei, and J. Yang, European Physical Journal D **70**, 262 (2016).
[56] N. Mielec, M. Altorio, R. Sapam, D. Horville, D. Holleville, L. A. Sidorenkov, A. Landragin, and R. Geiger, Appl. Phys. Lett. **113**, 161108 (2018).
[57] R. Tycko, A. Pines, and J. Guckenheimer, J. Chem. Phys. **83**, 2775 (1985).
[58] S. Odedra and S. Wimperis, Journal of Magnetic Resonance **214**, 68 (2012).
[59] B. Luy, K. Kobzar, T. E. Skinner, N. Khaneja, and S. J. Glaser, Journal of Magnetic Resonance **176**, 179 (2005).
[60] M. H. Levitt, J. Chem. Phys. **128**, 052205 (2008).
[61] M. Braun and S. J. Glaser, New Journal of Physics **16**, 115002 (2014).
[62] A. J. Shaka, J. Keeler, T. Frenkiel, and R. Freeman, Journal of Magnetic Resonance (1969) **52**, 335 (1983).
[63] M. Carey, M. Belal, M. Himsworth, J. Bateman, and T. Freegarde, Journal of Modern Optics **65**, 657 (2018).
[64] M. Kasevich, D. S. Weiss, E. Riis, K. Moler, S. Kasapi, and S. Chu, Phys. Rev. Lett. **66**, 2297 (1991).
[65] In practice, the time required for the AWG to respond to a hardware trigger is determined by the sample rate. We therefore oversample waveforms, so that each ϕ_n comprises many "subsamples" of equal phase, in order to keep the AWG sample period much less than the ~ 100 ns rise-time of the AOM that shutters the Raman beams.
[66] A. Dunning, *Coherent atomic manipulation and cooling using composite optical pulse sequences*, Ph.D. thesis, University of Southampton, UK (2014).
[67] P. Gillot, B. Cheng, S. Merlet, and F. Pereira Dos Santos, Phys. Rev. A **93**, 013609 (2016).
[68] M. H. Goerz, E. J. Halperin, J. M. Aytac, C. P. Koch, and K. B. Whaley, Phys. Rev. A **90**, 032329 (2014).